Proceedings of the Thirty-fourth (2024) International Ocean and Polar Engineering Conference **www.isope.org**
Rhodes, Greece, June 16–21, 2024
Copyright © 2024 by the International Society of Offshore and Polar Engineers (ISOPE)
ISBN 978-1-880653-78-4; ISSN 1098-6189

Numerical Study of Flow Structure and Air Entrainment around a Shallowly Submerged Hydrofoil

Yuming Shao[1], Wentao Wang[1,2], Jianhua Wang[1], Decheng Wan[1]*

[1] Computational Marine Hydrodynamics Lab (CMHL), School of Ocean and Civil Engineering,
Shanghai Jiao Tong University, Shanghai, China
[2] China Ship Scientific Research Center, Wuxi, China

[*]Corresponding Author

ABSTRACT

The shallowly submerged hydrofoil often induces disturbances on the free surface, involving various physical phenomena and mechanisms. In this paper, we analyze the flow field around the hydrofoil under two different initial water depth conditions, revealing the suppression of wave height on the free surface as the hydrofoil approaches. The study indicates two gas entrainment mechanisms when the wave breaks. A quasi-steady state is observed for both the total entrained volume and quantity of entrained bubbles. The vortical wake of the hydrofoil leads to the rapid disappearance of large air bubbles, causing a shift in the power-law exponent of bubble number density from -10/3 to -9/2 as bubble diameter increases.

KEY WORDS: Free-surface flows; hydrofoil; wave breaking; air entrainment; bubble dynamics; vortex interactions

INTRODUCTION

Wave breaking and air entrainment are intense two-phase interface interaction phenomena, influencing the mass and momentum exchange between air and water(Deike et al., 2022). This phenomenon is particularly prevalent in coastal and ocean engineering. Waves undergo fragmentation when interacting with marine structures, entraining significant amounts of air into the water, thereby generating copious amounts of white foam near the vicinity of marine structures. Navigating ships experience energy losses during this process, and marine platform columns and subdecks are subject to impacts that may lead to structural damage. These reasons have brought increasing scholarly attention to the phenomenon of wave breaking in recent years. However, due to the complexity of wave breaking and the turbulence generated post-breakage, this research has consistently posed significant challenges.

It is difficult to capture and measure wave breaking under laboratory conditions. Some scholars (Deane et al., 2002; Leifer et al., 2006) have employed optical and acoustic techniques to measure the size distribution of bubbles beneath breaking waves, yet a more detailed analysis of the bubbles remains lacking. Recently, Zhang et al.(2023) have developed an innovative and scalable oscillating bubble dynamics theory, starting from fundamental mathematical principles and physical equations. This theory has the capability to simultaneously consider various complex physical factors, including boundaries, interactions between bubbles, surrounding flow fields, gravity, bubble migration, compressibility of the fluid, viscosity, and surface tension. In addition, with advancements in computational power and numerical methods, studying wave breaking through numerical simulations has become feasible. Wang et al. (2016) conducted numerical simulations of three-dimensional wave breaking using a uniform Cartesian grid with a total grid count of 12 billion, revealing the formation process of entrained bubbles and liquid droplets during wave breaking. To further reduce the demand for computational resources, scholars have developed Adaptive Mesh Refinement (AMR) technology, dynamically refining grids in critical areas of the flow field by specifying variations in physical quantities. Deike et al. (2015) employed AMR technology in conjunction with DNS numerical simulation methods to numerically simulate two-dimensional wave breaking phenomena, investigating the overall volume of air entrained and the distribution of bubble sizes during the overturning wave breaking process. Numerous scholars (Erinin et al., 2023; Li et al., 2022) have concluded that the size distribution of bubble clusters generated by wave breaking follows a power-law distribution, represented as bubble number density $N(r) \propto r^{-m}$, where $m \in [2.5 : 3.5]$, r is the bubble radius. Some experiments and numerical simulations explicitly indicate that the Hinze scale of wave-breaking bubbles is approximately 1 mm. Bubbles larger than the Hinze scale undergo shear fragmentation due to turbulence, with a power exponent of -10/3. Bubbles smaller than the Hinze scale are dominated by flow instability induced by surface tension, with a power exponent of -3/2.

The phenomenon of wave breaking induced by structures traversing a free liquid surface has been extensively studied through various experiments and numerical simulations (Erinin et al., 2023; Li et al.,

2022). However, these studies typically focus on statistically averaging macroscopic quantities such as free surface wave height and velocity distribution. There is a current lack of corresponding research regarding the generation, evolution, and interaction of bubbles with the turbulent flow field during the free surface breaking process. Hu et al. (2021) conducted numerical simulations on the wave breaking near a surface-piercing plate. He delved into the characteristics of the evolution of underwater bubble clusters and the spatial and size distribution of bubbles under different incident flow angles. Li et al. (2021) employed LES simulations to investigate the phenomenon of wedge-shaped water leaps occurring beneath a surface-piercing hydrofoil during towing. He analyzed the dynamic behavior of entrained bubble clusters under conditions with large-scale coherent structures such as vertical shear vortices and spanwise vortices, providing insights into the dynamics and two-phase turbulence characteristics.

On the other hand, when a submerged structure approaches the free liquid surface, the free surface undergoes deformation and breaking due to the influence of the turbulent flow field surrounding the structure. Previously, submerged cylinders have been the focus of numerous scholarly investigations. Colagrossi et al. (2019) conducted an analysis of the forces acting on cylinders and the variations in the free surface under different incoming flow velocities using the Smoothed Particle Hydrodynamics method. Additionally, Hendrickson et al. (2022) studied the bubble entrainment resulting from the disturbance of the free surface by a rotating cylinder, proposing the entrainment model applicable to the complex periodic shedding of vortices that leads to bubble entrainment. Guo et al. (2023) employed a two-dimensional adaptive mesh to analyze entrainment and bubbles around a rotating cylinder, further revealing the interaction between vortices and bubbles.

The investigation of free surface breaking induced by fully submerged hydrofoils was initially conducted by Duncan et al. (1983) through experiments. However, due to experimental constraints, the focus primarily shifted towards the evolution of the free surface when hydrofoils were positioned at varying depths. Prasad et al. (2015) employed the RNAS turbulence model to study the lift and drag of NACA0012 hydrofoils at six different water depths. They observed significant fluctuations in lift and drag when the interface was broken. Jin et al. (2021) explored the characteristics of free surface breaking caused by NACA0024 hydrofoils, providing statistical analysis of turbulence intensity and energy dissipation downstream. Their findings revealed that wave breaking resulted in a 12% dissipation of total energy. In previous studies, the focus has primarily centered on the discussion of macroscopic forces and the evolution of velocity and pressure fields around partially submerged structures at varying water depths. However, a more in-depth analysis of two-phase flow phenomena, such as free-surface breaking waves and the subsequent entrainment of air, has been lacking in these investigations.

This study represents an extension of previous research, employing non-dimensionalized parameters to investigate the disturbances of hydrofoils on the free surface at various water depths. This study aims to analyze the flow structure of wave breaking around a shallowly submerged hydrofoil, including entrainment of bubbles, and the interaction between bubbles and turbulent vortices. The organization of this paper is as follows. The mathematical model of the numerical method is firstly introduced. Then the computation conditions of the hydrifoil model is demonstrated. The results are finally discussed and summarized.

NUMERICAL METHOD

This paper is based on the open source software Basilisk flow solver (Popinet et al., 2018), which is a development of Gerris (Popinet et al., 2009) and has been verified in polyphase problems, such as wave breaking, jet, bubble rising.

Governing Equations

For incompressible, variable density N-S equations with surface tension can be described as:

$$\rho(\partial_t \boldsymbol{u} + (\boldsymbol{u}\cdot\nabla)\boldsymbol{u}) = -\nabla p + \nabla\cdot(2\mu\boldsymbol{D}) + \rho\mathbf{g} + \boldsymbol{f}_\sigma \tag{1}$$

$$\partial_t \rho + \nabla\cdot(\rho\boldsymbol{u}) = 0 \tag{2}$$

$$\nabla\cdot\boldsymbol{u} = 0 \tag{3}$$

Where $\boldsymbol{u} = (u, v, w)$ is the velocity of the fluid, $\rho \equiv \rho(x,t)$ is the density of the fluid, p represents the pressure, $\mu \equiv \mu(x,t)$ is the dynamic viscosity coefficient, $\boldsymbol{D}$ is the deformation coefficient, Defined as $D_{ij} \equiv (\partial_i u_j + \partial_j u_i)/2$.

Interface Capturing Method

The Basilisk flow solver employs the Momentum-Conserving Volume-Of-Fluid (MCVOF) method to trace phase interfaces (Fuster et al., 2018). The fluid's volume fraction field is reconstructed using the Piecewise Linear Interface Construction (PLIC) method, and the normal direction of the interface is determined by the Mixed-Youngs-Centered (MYC) method (Youngs, 1982).

$$\rho(\alpha) = \rho_1\alpha + \rho_2(1-\alpha) \tag{4}$$

$$\mu(\alpha) = \mu_1\alpha + \mu_2(1-\alpha) \tag{5}$$

Where ρ_1, ρ_2, μ_1, μ_1 represent the density and viscosity of the two fluids. Then the density convection equation of Eq. 2 can be replaced by the equivalent volume fraction convection equation:

$$\partial_t \alpha + \nabla\cdot(\alpha\mathbf{u}) = 0 \tag{6}$$

Surface tension calculation method

In the traditional VOF method, the surface tension term $\boldsymbol{f}_\sigma$ in Eq. 1 is usually obtained from the volume fraction:

$$\boldsymbol{f}_\sigma = \sigma\kappa(\alpha)\delta_s\boldsymbol{n} \tag{7}$$

Where σ is the surface tension coefficient, δ_s is the Dirac function of the interface, indicating that the surface tension term acts on the interface, and $\boldsymbol{n}$ is the normal of the interface.
Free surface curvature $\kappa(\alpha)$:

$$\kappa(\alpha) = -\nabla\left(\frac{\nabla\alpha}{|\nabla\alpha|}\right) \tag{8}$$

However, the volume fraction α is discontinuous at the free surface, so there will be an error in calculating the curvature. In this study, the continuous function Level Set method is used to calculate the surface tension term

$$\boldsymbol{f}_\sigma = \sigma\kappa(\phi)\delta_s\boldsymbol{n} \tag{9}$$

Therefore, it is also necessary to solve the transport equation of the level set function ϕ:

$$\partial_t \phi + \nabla \cdot (\alpha \phi) = 0 \tag{10}$$

Where ϕ is defined as the sign distance function of the free surface:

$$\begin{cases} \phi < 0 & Air\ phase \\ \phi = 0 & Free\ surface \\ \phi > 0 & Liquid\ phase \end{cases} \tag{11}$$

This method is called CLSVOF (Coupled Level Set and Volume of Fluid) (Limare et al., 2023), which can combine the advantages of both VOF and Level Set methods, not only has good mass conservation, but also gives more accurate interface geometry information. The coupling mode of these two methods in this study is shown in Fig. 1 below

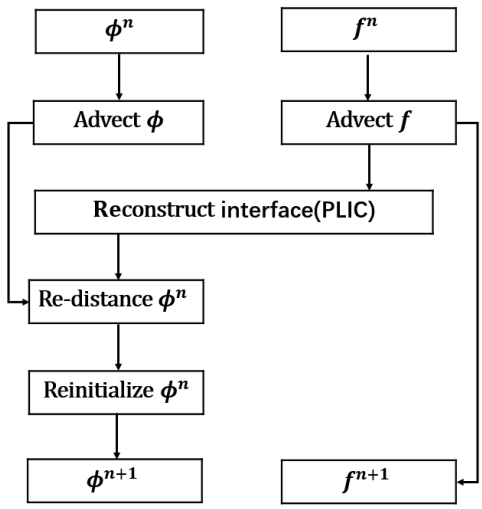

Fig. 1 Flow chart of the CLSVOF method

COMPUTATIONAL CONDITIONS

Computational set-up

The 2D computational domain for this study is illustrated in Fig. 2. The origin of the coordinate axes is defined at the leading edge of a NACA0012 hydrofoil with a 5-degree angle of attack. The whole computational domain is sized at $30c \times 30c$, which is set according to the multiple of the string length c ($c = 1\,m$). The free surface is positioned at a height h above the hydrofoil. The inlet is configured as a Dirichlet velocity boundary, located 10c away from the hydrofoil to mitigate the influence of the incoming flow boundary. The outlet is set with Neumann conditions, situated 19c from the hydrofoil to allow for the adequate development of the bubble wake. Both the Top and Bottom boundaries are assigned no-slip conditions, positioned 15c from the hydrofoil.

This study will conduct numerical simulations for five different water depth conditions with h/c ratios of 0.5 and 1.1. The incoming flow velocity is set to $U = 1.789\ \mathrm{m/s}$, corresponding to Froude number $\mathrm{F_{nc}} = U/\sqrt{gc} = 0.571$ and Reynolds number $\mathrm{Re_{nc}} = \rho U c/\mu = 1.569 \times 10^6$. The ratio of dynamic viscosity between air and water is $1.784 \times 10^{-5}/1.138 \times 10^{-3}$, with a density ratio of 1/998. The gravitational acceleration is denoted as $g = 9.81\ \mathrm{m/s^2}$, and the surface tension coefficient is set to 0.07 N/m.

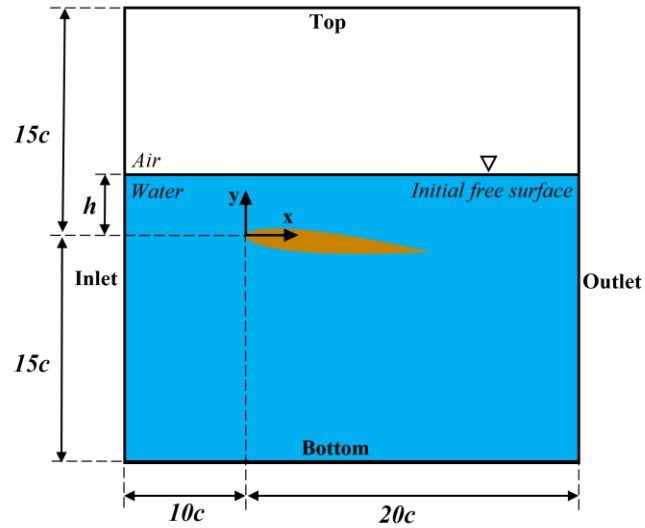

Fig. 2 Physical model and related geometric parameters at the initial time

Grid convergence verification

This study employs adaptive mesh refinement technology, where the grid resolution corresponds to $\Delta_{min} = 30\mathrm{c}/2^{l_{max}}$, l_{max} representing the defined maximum refinement level. The simulations in this study are conducted for three refinement levels: $l_{max} = 11(\Delta_{min} = \mathrm{c}/68)$, $l_{max} = 12(\Delta_{min} = \mathrm{c}/136)$ and $l_{max} = 13(\Delta_{min} = \mathrm{c}/272)$, depicting the flow around a shallow-water hydrofoil. The velocity field is denoted as $u_{err} = 0.02$, and the volume fraction is set as $\alpha_{err} = 1e - 18$. The maximum Courant–Friedrichs–Lewy (CFL) number is set to 0.2.

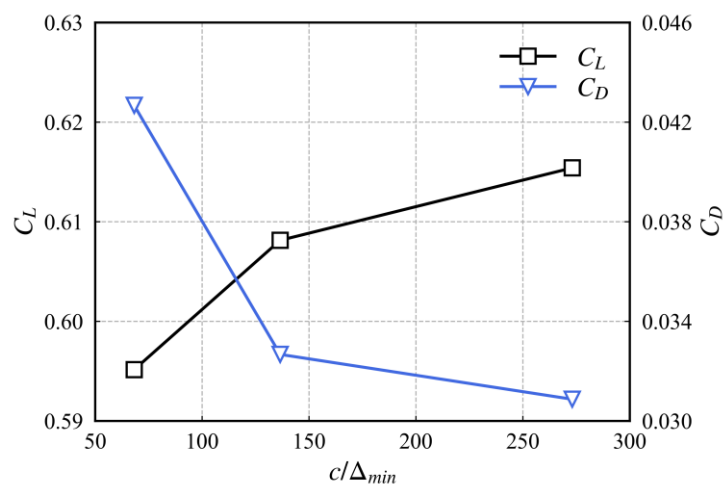

Fig. 3 Lift and drag coefficients

The operating conditions are set according to Duncan et al. (1983), with $\mathrm{h/c} = 1.03$ and $\mathrm{c} = 0.2$. Figure 3 depicts the computational results for three grid resolutions. As the grid resolution increases, the lift coefficient gradually increases, and the drag coefficient gradually decreases, with both trends exhibiting a diminishing rate of change. Table 1 presents the computational results at three resolutions alongside results from other study. Upon comparison, the lift and drag coefficients for $l_{max} = 11$ and $l_{max} = 12$ fall between the computed results by Prasad et al. (2015) and

Pernod et al. (2023). Therefore, it can be inferred that the results for $l_{max} = 11$ and $l_{max} = 12$ have converged.

Table 1. Comparison of lift and drag coefficients

	C_L	C_D
Present work($l_{max} = 11$)	0.5952	0.0327
Present work($l_{max} = 12$)	0.6081	0.0313
Present work($l_{max} = 13$)	0.6154	0.0309
Prasad et al., 2015	0.6347	0.0355
Pernod., 2023	0.6127	0.0265

Figure 4 presents a comparative analysis between numerical results and experimental findings for the free surface at $l_{max} = 12$. The results exhibit a substantial alignment between numerical and experimental outcomes. The primary discrepancy manifests in the slightly lower positioning of the numerical peaks compared to the experimental results. This phenomenon aligns with the findings of Prasad et al. (2015) and is primarily attributed to the shoaling effect resulting from the limited tank height in the experiment.

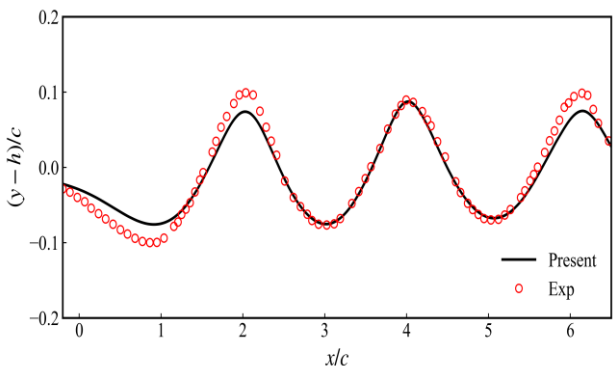

Fig. 4 Lift and drag coefficients

To better capture the bubble dynamics, this study opts for $l_{max} = 12$ in the numerical investigations. As depicted in Fig. 5， corresponding to the moment of the first impact of waves on the free surface, the adaptive strategy employed in this study effectively enhances grid resolution, particularly in regions characterized by significant free surface variations and the vortical wake downstream of the hydrofoil.

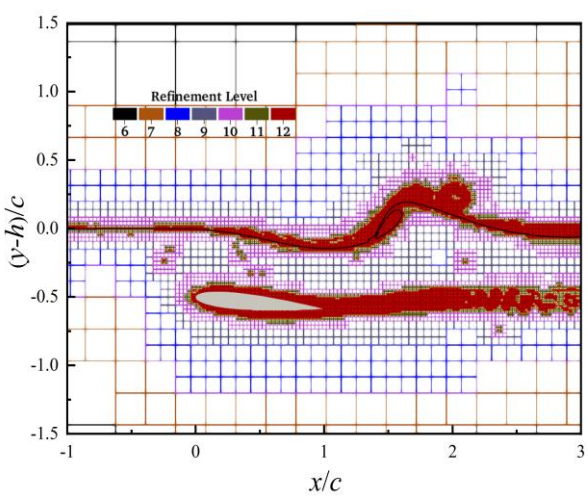

Fig. 5 Grid adaptive refinement diagram

RESULTS AND DISCUSSION

Flow field comparison

Figure 6 illustrates the free-surface profiles for two different conditions: $h/c = 1.1$ and $h/c = 0.5$. From the figure, it is observed that under the $h/c = 1.1$ condition, the free surface does not exhibit significant fragmentation. However, in the region where $x/c < 10$ regular wave patterns are formed, while beyond $x/c > 10$ the undulations of the wave surface become irregular. For the $h/c = 0.5$ condition, a distinct region of intense gas-liquid mixing and wave-breaking forms at the top of the hydrofoil, with a considerable amount of air entrained in the water. This entrained air rolls downstream, and larger bubbles decompose into numerous smaller ones. While some of these bubbles rise and escape through the free surface, others, due to reduced buoyancy and surface tension preventing further fragmentation, are carried downstream by the incoming flow.

Figure 7 presents vorticity diagram for two conditions, $h/c = 1.1$ and $h/c = 0.5$. In the case of $h/c = 1.1$, a notable feature is the upward spreading of the hydrofoil's vortex wake interacting with the free surface, leading to the accumulation of vorticity on the free surface in the region $x/c > 10$. Eventually, this vorticity accumulation disperses into the air downstream, providing an explanation for the irregularities observed in the downstream wave surface for $h/c = 1.1$. This phenomenon appears more pronounced in the $h/c = 0.5$ condition, where the hydrofoil is closer to the free surface, making its vortex wake more influential. Numerous positive and negative vortices are observed on the free surface, leading to repetitive fragmentation and noticeable suppression of wave height. Additionally, the free surface evidently affects the hydrofoil. Comparing the vorticity diagram for the two conditions, it is evident that, under $h/c = 0.5$, the hydrofoil 's wake vortices exhibit a higher alternating frequency and a smaller spreading range, indicating a more rapid dissipation of turbulence induced by the hydrofoil.

Bubble dynamic performance analysis

To investigate the dynamics of entrained gas, we conducted further analysis on the bubbles under the condition of $h/c = 0.5$.

Figure 8 illustrates the temporal variation of the total volume of entrained gas, with both time and total volume presented in dimensionless units. From the figure, the initial volume change occurs at $t = 7.3$. At this point, the hydrofoil induces the first overturning and breaking of waves at the top of the hydrofoil, creating a large cavity through entrainment. Subsequently, as this cavity breaks and develops downstream, the jet continues to entrain gas. The inflow velocity decreases in this disturbed region, causing a sustained increase in wave height after each breakage. When the wave height reaches a certain threshold, a continued overturning and breaking occur, resulting in a sharp peak in the total volume curve, as observed at $t = 77.3$. Each peak corresponds to Plunging wave breaking, while the troughs indicate the upward escape of large air bubbles. Despite the continuous pulsations in the overall bubble volume curve, its mean value remains around 0.02.

Figure 9 shows the variation in the number of entrained bubbles over time. The overall number of bubbles exhibits a consistent oscillation, hovering around 78. In comparison to Fig. 7, the positions of extremities in Fig. 8 are slightly delayed. The delay in the occurrence of peak values can be attributed to the fact that it takes some time for a larger gas tend to break into smaller bubbles after being entrapped. Similarly, the delay

in reaching trough values is due to the faster rising speed and lower quantity of large bubbles compared to smaller ones. Therefore, the decrease in the volume of entrained gas is reflected in the number of entrapped bubbles with a noticeable delay.

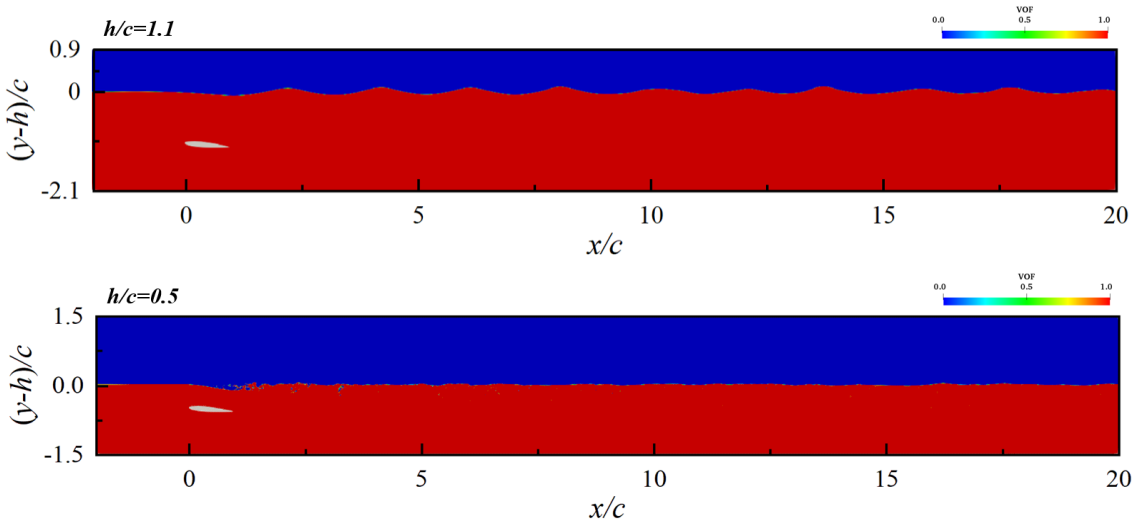

Fig. 6 Instantaneous free surface profiles at t=170

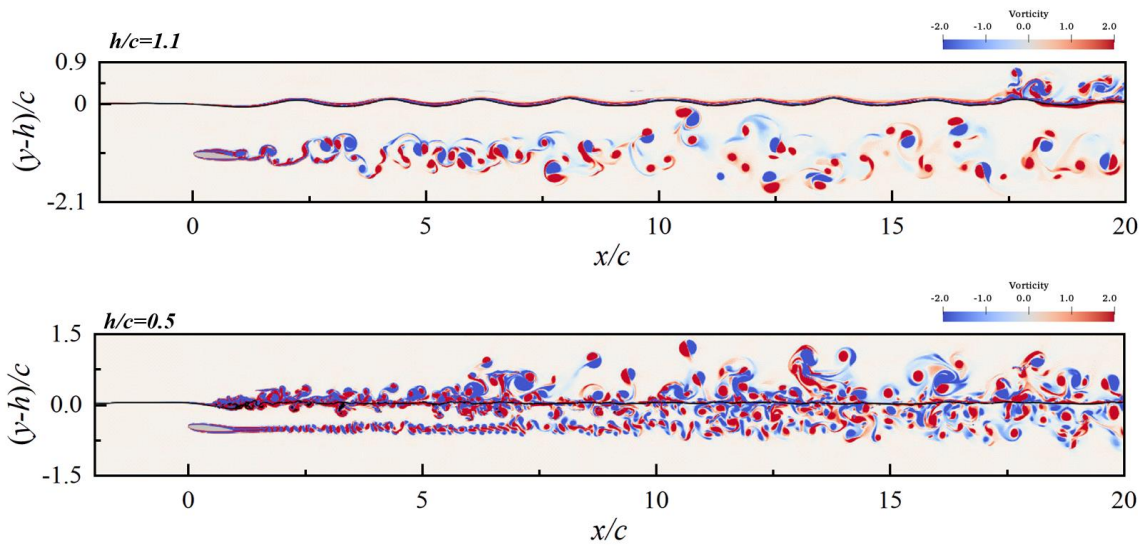

Fig. 7 Instantaneous vorticity diagram at t=170

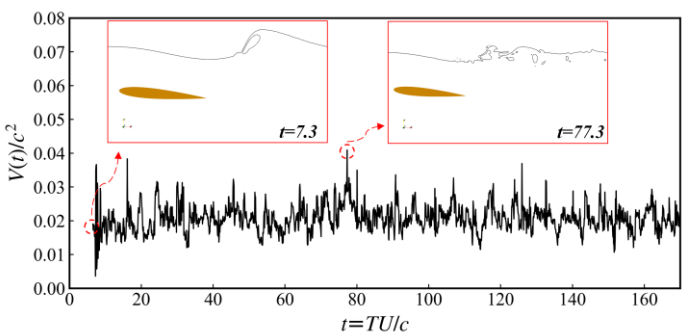

Fig. 8 The curves of bubble volume over time

Figure 10 presents the time-averaged size distribution of bubbles, expressed as the particle size spectrum $\bar{N}(r_{\text{eff}}) = \frac{1}{T}\int_t^{t+T} \frac{n(r_{\text{eff}},b)}{b} dt$ per bin size b where r_{eff} represents the equivalent radius. From the figure, it is evident that the bubble size spectrum predominantly follows a power-law distribution, indicating that turbulent shear fragmentation is the predominant mechanism governing the formation of bubble clusters. However, in contrast to classic wave breaking problems (Deike et al., 2022), as the bubble radius increases, the bubble count diminishes, and the power-law exponent gradually deviates from -10/3.

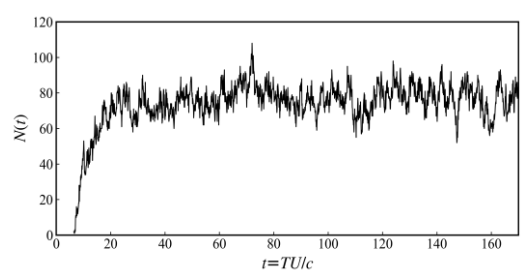

Fig. 9 The curves of bubble number over time

This phenomenon is primarily attributed to the intense interaction between large-scale quasi-coherent vortices generated by the flow separation at the wake section of the hydrofoil and the bubble interface, leading to rapid shear-induced fragmentation of larger bubbles or cavities with shorter residence times. Consequently, the power-law exponent in the region of large bubble sizes approaches -9/2. This observation is similar to the distribution of bubbles generated by the flow around structures piercing the free surface (Hendrickson,2019; Li et al., 2021).

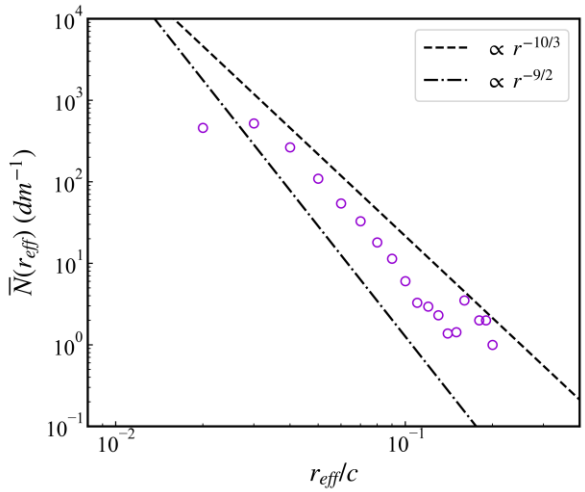

Fig. 10 Time-averaged bubble particle size spectrum

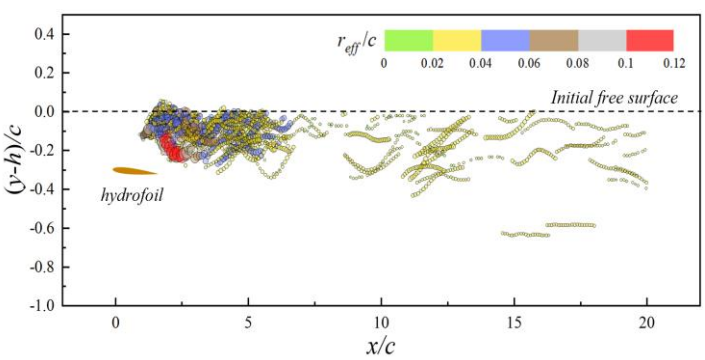

Fig. 11 Bubble spatial distribution at t=40

Figure 11 gives the spatial distribution of bubbles at the typical moment $t = 40$. The primary concentration of larger bubbles is observed predominantly in the region atop the hydrofoil, coinciding with the area where entrainment is most pronounced. In the region $0 < x/c < 5$ larger bubbles swiftly rise and break into smaller ones. As these smaller bubbles progress downstream with the flow, between $10 < x/c < 15$, some bubbles exhibit an upward trend in response to the upwelling vortical structures in the wake of the hydrofoil. In comparison to the larger bubbles, smaller bubbles with lower buoyancy, persist in the water for an extended duration and cover a broader range of motion.

CONCLUSIONS

In this paper, we simulate the flow structure around a submerged hydrofoil near the free surface. Previous studies primarily focused on lift and drag of the hydrofoil under different water depths. This research delves into the phenomenon of wave breaking induced by the hydrofoil at $h/c = 0.5$ and $h/c = 1.1$, providing further analysis of the entrapped air volume, bubble count, number density, and spatial distribution. The key findings are as follows:

1) The presence of the hydrofoil generates regular waves on the free surface. However, as the hydrofoil approaches the free surface, wave heights are suppressed, leading to more pronounced wave breaking phenomena.
2) Air entrainment has two main sources: firstly, the blocking effect of the hydrofoil induces a velocity difference between the free surface and hydrofoil, resulting in air entrainment. Secondly, vortices in the wake of the hydrofoil spread to the free surface, perturbing it and causing air entrainment.
3) Analysis of bubble dynamics reveals periodic fluctuations in both total volume and count due to entrainment, yet they exhibit a quasi-steady state. Additionally, examining the spatial distribution of bubbles indicates that, influenced by the vortical structures in the wake, larger bubbles in the wake dissipate quickly, leading to a power-law exponent shift from -10/3 to -9/2 as bubble diameter increases.

Future work will explore hydrofoil conditions under various water depths to reveal the relationship between air entrainment dynamics and immersion depth. Furthermore, since air entrainment often involves rich three-dimensional effects, further investigations in three-dimensional conditions are essential for a comprehensive understanding of the phenomenon.

ACKNOWLEDGEMENTS

This work is supported by the National Natural Science Foundation of China (52131102), to which the authors are most grateful.

REFERENCES

Colagrossi, A., Nikolov, G., Durante, D., Marrone, S., and Souto-Iglesias, A. (2019). "Viscous flow past a cylinder close to a free surface: Benchmarks with steady, periodic and metastable responses, solved by meshfree and mesh-based schemes," *Computers and Fluids*, 181, 345-363.

Deane, G. B., and Stokes, M. D. (2002). "Scale dependence of bubble creation mechanisms in breaking waves," *Nature*, 418(6900), 839-844.

Deike, L. (2022). "Mass transfer at the ocean–atmosphere interface: the role of wave breaking, droplets, and bubbles," *Annual Review of Fluid Mechanics*, 54, 191-224.

Deike, L., Popinet, S., and Melville, W. K. (2015). "Capillary effects on wave breaking," *Journal of Fluid Mechanics*, 769, 541-569.

Duncan, J. H. (1983). "The breaking and non-breaking wave resistance of a two-dimensional hydrofoil," *Journal of fluid mechanics*, 126, 507-520.

Erinin, M. A., Liu, X., Wang, S. D., and Duncan, J. H. (2023). "Plunging breakers. Part 1. Analysis of an ensemble of wave profiles," *Journal of Fluid Mechanics*, 967, A35.

Fuster, D., Popinet, S. (2018). "An all-Mach method for the simulation of bubble dynamics problems in the presence of surface tension," *Journal of Computational Physics*, 374: 752-768.

Guo, C., Ji, M., Han, Y., Liu, T., Wu, Y., and Kuai, Y. (2023). "Numerical simulation of the horizontal rotating cylinder and the air entrainment near the free surface," *Physics of Fluids*, 35(9).

Hendrickson, K., and Yue, D. K. (2019). "Structures and mechanisms of air-entraining quasi-steady breaking ship waves," *Journal of Ship Research*, 63(02), 69-77.

Hendrickson, K., Weymouth, G. D., Yu, X., and Yue, D. K. P. (2019). "Wake behind a three-dimensional dry transom stern. Part 1. Flow structure and large-scale air entrainment," *Journal of Fluid Mechanics*, 875, 854-883.

Hendrickson, K., Yu, X., and Yue, D. K. (2022). "Modelling entrainment volume due to surface-parallel vortex interactions with an air–water interface," *Journal of Fluid Mechanics*, 938, A12.

Hu, Y., Liu, C., Hu, C., and Wan, D. (2021). "Numerical investigation of flow structure and air entrainment of breaking bow wave generated by a rectangular plate," *Physics of Fluids*, 33(12).

Jin, Q., Hudson, D., Temarel, P., and Price, W. G. (2021). "Turbulence and energy dissipation mechanisms in steady spilling breaking waves induced by a shallowly submerged hydrofoil," *Ocean Engineering*, 229, 108976.

Leifer, I., and De Leeuw, G. (2006). "Bubbles generated from wind‐steepened breaking waves: 1. Bubble plume bubbles," *Journal of Geophysical Research: Oceans*, 111(C6).

Li, Z., Liu, C., Wan, D., and Hu, C. (2021). "High-fidelity simulation of a hydraulic jump around a surface-piercing hydrofoil," *Physics of Fluids*, 33(12).

Li, Z., Zhang, X. S., and Wan, D. C. (2022). "Research progress on the hydrodynamic performance of water-air-bubble mixed flows around a ship," *Journal of Hydrodynamics*, 34(2), 171-188.

Limare, A., Popinet, S., Josserand, C., Xue, Z., and Ghigo, A. (2023). "A hybrid level-set/embedded boundary method applied to solidification-melt problems," *Journal of Computational Physics*, 474, 111829.

Pernod, L., Sacher, M., Wackers, J., Augier, B., and Bot, P. (2023). "Free-surface effects on two-dimensional hydrofoils by RANS-VOF simulations," *Journal of Sailing Technology*, 8(01), 24-38.

Popinet, S. (2009). "An accurate adaptive solver for surface-tension-driven interfacial flows," *Journal of Computational Physics*, 228(16), 5838-5866.

Popinet, S. (2018). "Numerical models of surface tension," *Annual Review of Fluid Mechanics*, 50, 49-75.

Prasad, B., Hino, T., and Suzuki, K. (2015). "Numerical simulation of free surface flows around shallowly submerged hydrofoil by OpenFOAM," *Ocean Engineering*, 102, 87-94.

Wang, Z., Yang, J., and Stern, F. (2016). "High-fidelity simulations of bubble, droplet and spray formation in breaking waves," *Journal of Fluid Mechanics*, 792, 307-327.

Wu, D., Wang, J., Wan, D. (2021). "Delayed detached eddy simulation method for breaking bow waves of a surface combatant model with different trim angle," *Ocean Engineering*, 242, 110177.

Yang, Y., Hu, Y., Liu, C., Gao, R., and Hu, C. (2023). "Wake and air entrainment properties of transom stern over a wide range of Froude numbers," *Physics of Fluids*, 35(6).

Youngs, D. L. (1982). "Time-dependent multi-material flow with large fluid distortion," *Numerical methods for fluid dynamics*.

Zhang, A., Li, S. M., Cui, P., Li, S., and Liu, Y. L. (2023). "A unified theory for bubble dynamics," *Physics of Fluids*, 35(3).